Numerical analysis on effect of furnace scale on heat transfer mechanism of coal particles in pulverized coal combustion field

Nozomu HASHIMOTO[1,2] and Hiroaki WATANABE[1,3]

1. Central Research Institute of Electric Power Industry (CRIEPI), 2-6-1 Nagasaka, Yokosuka, 240-0196 Japan
2. Hokkaido University, Kita 13, Nishi 8, Kita-ku, Sapporo, 060-8628 Japan
3. Kyushu University, 744 Motooka, Nishi-ku, Fukuoka, 819-0395 Japan

Correspondence: Nozomu HASHIMOTO
Laboratory of Space Utilization, Division of Mechanical and Space Engineering, Graduate School of Engineering, Hokkaido University, Kita 13, Nishi 8, Kita-ku, Sapporo, 060-8628 Japan
Phone: +81-11-706-6386
FAX: +81-11-706-6386
E-mail: nozomu.hashimoto@eng.hokudai.ac.jp

Abstract

To investigate the effect of the furnace scale on the heat transfer mechanism of coal particles, numerical simulations of coal combustion fields in three different scale furnaces (915 MW_{th} actual large scale boiler, 2.4 MW_{th} and 0.76 MW_{th} test furnaces) were conducted. High accuracy of simulation methods was validated with the measured data. From the comparison of numerical simulations between three different scale furnaces, it was clarified that the particle residence time with high particle temperature for a small scale furnace is shorter than that for a large scale furnace even if the particle residence time passing the high temperature gas is the same. This is caused by the insufficient heat gain of particles for a small scale furnace due to the lower radiation heat transfer because of the thinner flame thickness in the small furnace. The sphericity of ash particles from small scale furnaces is lower than that for large scale furnaces due to the shorter particle residence time with high particle temperature. These findings should be considered when the usability of coal brands for actual large scale boilers is evaluated by the fly ash properties from a small scale experimental furnace.

Key words: coal combustion; numerical simulation; boiler; furnace scale; heat transfer mechanism; particle

Nomenclature

$D_{s\text{-}ash}$: surface mean diameter, μm

h: time-averaged convection heat transfer coefficient, kW/(m^2 K)

HG_{rad}: integrated heat gain of particles by radiation heat transfer normalized by initial particle mass, MJ/kg

$HL_{dev,1750K}$: integrated heat loss of particles by devolatilization while the particles are passing gas with temperature above 1750 K normalized by initial particle mass, MJ/kg

$Q_{net,1750K}$: net heat gain of particles while the particles are passing gas with temperature above 1750 K normalized by initial particle mass, MJ/kg

S_{Ab}/S_{Ad}: reciprocal Carman's shape factor

$t_{p,1750K}$: particle residence time with particle temperature above 1750 K, s

$t_{g,1750K}$: particle residence time passing gas with temperature above 1750 K, s

1. Introduction

Pulverized coal combustion is introduced in a large part of coal-fired thermal power plants in the world. Even though the fundamental technology for pulverized coal combustion was established many decades ago, many types of problems, e. g., fouling, slagging, sulfidation corrosion, increase in particulate matter and NOx concentrations in exhaust gas and increase in unburned carbon in fly ash, occur in the operation of coal-fired furnaces. To solve the problems described above, understanding of the gas flow pattern, temperature distribution, gas species concentration distributions and coal particle behavior in the furnace is very important. However, the phenomena described above are largely affected by the design of furnaces. Numerical simulation is a powerful tool for understanding such phenomena in each furnace with a different design. Recently, numerical simulations of pulverized coal combustion field in large-scale furnaces have been conducted by various research groups [1-9]. For numerical simulations of pulverized coal combustion, simplified models are generally employed because of the limitation of computational resources. However, sometimes employing such simplified models causes relatively large errors in prediction of the phenomena in the furnaces. In Central Research Institute of Electric Power Industry (CRIEPI), new models such as the TDP model for detailed devolatilization modeling [10, 11] and the RD model for detailed char combustion modeling [12] have been developed to improve the accuracy of the simulation of coal combustion. Since the development of new models require various experimental data to validate the simulation results, various studies have been conducted using test facilities in CRIEPI such as the studies for the combustion characteristics of sub-bituminous coal [13, 14], the combustion

characteristics of high ash coal [15, 16], the hydrogen sulfide formation in coal combustion field [17], the soot formation characteristics in coal combustion field [18], the influence of combustion condition and coal properties on physical properties of flay ash [19] and the detailed flow field in the coal combustion test furnace [20]. Experimental data from the facilities are also beneficial for the understanding of the coal combustion phenomena and the evaluation of coal brands for using in actual scale boiler. However, the thermal histories of coal particles in the experimental facilities can be different from that in the actual large scale boilers because the scale of flame can affect the heat transfer mechanism of the coal particles. Experimental apparatus with various sizes, e. g., the drop tube furnace (8-60 g-coal/h) [21, 22], the small coal jet burner (0.5 kg-coal/h) [11, 23], the triple stream burner (0.36-2.16 kg-coal/h) [24, 25], the RWTH furnace (6-7 kg-coal/h) [26, 27], the RWEn Combustion Test Facility (70 kg-coal/h) [28], the BEACH furnace (100 kg-coal/h) [13, 29, 30, 31], the IFRF furnace No. 1 (260 kg-coal/h) [32] and the MARINE furnace (300 kg-coal/h) [19, 33], have been used to investigate the coal combustion phenomena or to evaluate the combustion characteristics of various coal brands by some researchers. The difference in the thermal histories of coal particles should be considered to evaluate the usability of coal brands for actual large scale boilers by using the experimental data from small scale experimental apparatus. However, the effect of the furnace scale on the thermal histories of coal particles has not been clarified yet.

In this study, numerical simulations of coal combustion fields in three different scale furnaces (915 MW_{th} actual large scale boiler, 2.4 MW_{th} test furnace and 0.76 MW_{th} test furnace) were conducted to investigate the effect of the furnace scale on the heat transfer mechanism of coal particles. The

accuracy of the simulation result for the large scale boiler was validated by comparing with the measured data from the large scale boiler. After that, the calculated particle data from the simulation results of three furnaces were examined statistically in detail to investigate the effect of the furnace scale on the heat transfer mechanism.

2 Numerical simulation

2.1 Mathematical models and numerical method

The models for numerical simulations of pulverized coal combustion field employed in this study are the same as those of Hashimoto et al. [14]. The models for main phenomena are summarized in Table 1.

The gas-phase time-averaged continuity equation and conservation equations of the momentum, turbulent kinetic energy, dissipation, enthalpy and species are

$$\frac{\partial}{\partial x_i}\left(\rho_g u_i\right) = 0 \tag{2.1}$$

$$\frac{\partial}{\partial x_i}\left(\rho_g u_i \phi\right) = \frac{\partial}{\partial x_i}\left(\Gamma_\phi \frac{\partial \phi}{\partial x_i}\right) + S_\phi + S_{p\phi}\,, \tag{2.2}$$

where ϕ denotes the generalized variables expressing fluid velocity components u_i, the turbulent kinetic energy k, the rate of eddy dissipation ε, the fluid enthalpy h and the mass fractions of chemical species Y_i. Γ_ϕ denotes the turbulent exchange coefficient, and S_f and $S_{\mathrm{p}\phi}$ represent the

gas-phase source terms that are in addition to the convection and diffusion terms and the particle-phase source terms, respectively. The continuity and momentum equations were solved using the PISO algorithm [40].

The equation of motion for the representative coal particles is given by

$$m_p \frac{du_{pi}}{dt} = \frac{1}{2} C_d \rho_p A_p \mid u_{fi} - u_{pi} \mid (u_{fi} - u_{pi}) \qquad (2.3)$$

$$C_d = 24(1 + 0.15\,\mathrm{Re}_p^{0.687}) \big/ \mathrm{Re}_p \qquad (2.4)$$

$$\mathrm{Re}_p = D_p \mid u_{fi} - u_{pi} \mid \big/ \nu\,, \qquad (2.5)$$

where, m_p, u_{pi}, ρ_p, A_p, u_{fi} and ν are the particle mass (kg), the particle velocity component for direction i (m/s), the density of particle (kg/m^3), the projected area of particle (m^2), the fluid velocity component for direction i (m/s) and the kinematic viscosity of gas (m^2/s). The equation for the drag coefficient of solid particles (Eq. (2.4)) was taken from Schiller and Naumann [41].

The particle temperature T_p (K) was calculated by considering the heat transfer due to convection, radiation, heat loss due to the evaporation of moisture and the devolatilization reaction in coal particle, and heat gain due to char combustion, using the following equation:

$$m_p c_{p,p} \frac{dT_p}{dt} = -A_s h\left(T_p - T_g\right) + A_s \varepsilon_p \sigma\left(\Theta_R{}^4 - T_p{}^4\right) + \Delta h_{lat} \frac{dm_{p,w}}{dt} + \Delta h_{dev} \frac{dm_{p,v}}{dt} + \dot{q}_{char} \quad (2.6)$$

$$h = k_g Z\left(2 + 0.6\,\mathrm{Re}_p^{1/2}\,\mathrm{Pr}^{1/3}\right) \Big/ \left(e^Z - 1\right) D_p \quad (2.7)$$

$$Z = -c_{p,g}\left(dm_p/dt\right) \Big/ \pi D_p k_g \left(2 + 0.6\,\mathrm{Re}_p^{1/2}\,\mathrm{Pr}^{1/3}\right) \quad (2.8)$$

$$\Theta_R = \left(I/4\sigma\right)^{1/4}, \quad (2.9)$$

Here, $c_{p,p}$, A_s , ε_p and $\dot{q}_{\mathrm{char}}$ are the specific heat of particle (J/(kg K)), the surface area of particle (m^2), the absorptivity of particle, and the heat gain due to char combustion (J/s). In this study, the particle temperature was assumed to be uniform and the temperature distribution inside the particle was not considered because of the computational cost limitation. The equation for the heat transfer coefficient (Eq. (2.7)) was taken from El Wakil et al. [42]. The absorptivities of the coal particles and wall are assumed to be 0.85 and 0.4, respectively. Also, the absorption coefficient of the gas was set at 0.075 [29]. The interaction of the conserved properties between the gas phase and the coal particles was calculated by the particle-source-in cell (PSI-Cell) technique [43].

In this study, the modified TDP model [14] was employed for devolatilization of coal particle. The FLASHCHAIN model [44, 45] was used to produce the devolatilization database for the TDP model.

Gaseous combustion between the volatile matter and air was calculated using a combined model of

the kinetics and eddy dissipation models [36]. The chemical mechanism consists of the following two global reactions.

$$\mathrm{VM} + \alpha \mathrm{O_2} \rightarrow \beta \mathrm{CO} + \gamma \mathrm{H_2O} \tag{2.10}$$

$$\mathrm{CO} + \mathrm{O_2} \rightarrow \mathrm{CO_2} \tag{2.11}$$

In this study, the parameters for C_7H_8 oxidation proposed by Westbrook et al. [46] are employed for the rate parameters regarding the kinetics for Eq. (2.10). The parameters for CO oxidation proposed by Hautman et al. [47] are employed for the rate parameters regarding the kinetics for Eq. (2.11).

2.3. Computational domain and conditions

In this study, the numerical simulations for three furnaces, which are the 915 MW_{th} (350 MW_e) actual large scale boiler, the 2.4 MW_{th} and 0.76 MW_{th} test furnaces in CRIEPI, were conducted. The specification of the furnaces is shown in Table 2. The residence time in the furnace is about 4 s and the O_2 mole fraction at the furnace exit is 0.04 for all furnaces. The thermal input of the actual boiler is more than 300 times larger than that of the test furnaces.

Figure 1 shows the outlines of computational domains. Because the shape of the 915 MW_{th} is

bilaterally symmetric across the separate water wall, only the left half of the boiler was calculated. A symmetric condition was applied on the cross section at the center of furnace except for the separate water walls. Temperature outside the furnace was set by using the plant recorded data and thermal resistance was set to the value calculated from the conductivity and thickness of water wall or superheater tubes. The boundary conditions for the 2.4 MW_{th} and 0.76 MW_{th} test furnaces were set at the same conditions as in Ref. [33] and [10], respectively.

Table 3 shows the properties of the tested fuels. Two brands of coal, which are Coal A and B, were used in this study. The mixing ratio of Coal A and B was 70:30 on LHV basis for all furnaces. The mass fraction of moisture for coal particles supplied to the furnace is indicated as “Moisture (after pulverized)”. The difference in the moisture in the as-received basis and in the after pulverized basis was supplied as vaporized moisture in the primary air. It was assumed that the pulverized coal particles had initial diameters $D_{p,i}$ of 5, 20, 40, 60, 80 and 100 μm. Their mass fractions of the coal particles are set as shown in Table 3.

3 Results and discussion

3.1 Basic combustion characteristics in 915 MW_{th} large scale boiler

Figure 2 shows calculated streamlines in the 915 MW_{th} boiler. Colors of streamlines indicate (a) O_2 concentration and (b) gas temperature, respectively. It is observed that the streamlines are complexly intertwined with each other in the burner zone. In the superheater zone, on the other hand, the streamlines are not intertwined. This indicates that the mixing is not highly promoted in the

superheater zone. In other words, the degree of the completeness of mixing at the exit of the burner zone is very important for the operation of the large scale boiler. Because of the uncompleted mixing, an ununiformity of the O_2 concentration is observed in the burner zone (Fig. 2 (a)). In an analogous way, an ununiformity of the gas temperature is also observed in the burner zone (Fig. 2 (b)). It is observed that the ununiformity of the O_2 concentration is not resolved in the superheater zone. This is caused by that the space in the 915 MW_{th} boiler is so large that the mixing of gas concentrations is not promoted enough after the exit of the burner zone. On the other hand, the ununiformity of the gas temperature is resolved in the middle of superheater zone. This is considered due to that the number of mechanisms for uniforming the gas temperature is greater than that for uniforming the gas concentration, i.e., the radiative heat transfer as well as the convective and conductive heat transfers promotes the uniformization of the gas temperature, whereas only the convective and diffusive mass transfers promote the mixing of gas species.

Figure 3 shows the distributions of (a) gas temperature with velocity vectors and (b) O_2 concentration on the cross section at the center of center burners for the 915 MW_{th} boiler. The strong flow of hot burned gas from the front side to the rear side of the furnace is observed in Fig. 3 (a). This is caused by that the number of the burners on the front side is half again as much as that on the rear side. Because of this, the momentum of the hot burned gas from the front side burners is larger than that from the rear side burners. This is why the strong flow of the hot burned gas from the front side to the rear side is observed. Consequently, a low O_2 concentration area is observed at the rear side above the burner zone in Fig. 3 (b). This tendency is confirmed by the measured data as

explained in the next paragraph.

Figure 4 shows (a) the calculated O_2 concentration distribution on the furnace wall surface and (b) the comparison of O_2 concentration at the inspection windows on the furnace wall between the simulation result and the measured data for the 915 MW_{th} boiler. The circled numbers in Fig 4 (a) indicate the locations of the inspection windows. A low O_2 concentration area is observed on the rear side wall above the burner zone in Fig 4 (a). It should be noticed that the inspection window ② is located in the low O_2 concentration area. The low O_2 concentration on the rear side wall is confirmed by the measured data in Fig. 4 (b). Although there are some discrepancies between the simulation results and the measured data, the tendency that the O_2 concentration at the inspection window in the rear side of the furnace (② in Fig. 4 (b)) is lower than that at the other inspection windows is consistent. In other words, the simulation could qualitatively reproduce the tendency that the O_2 concentration on the rear side wall above the burner zone is lower than that at the front side.

Figure 5 shows the comparison of the quantity of heat transfer to the water wall, the plate and 2nd superheaters between the simulation result and the measured data. It can be confirmed that the discrepancies between the simulation result and the measured data are small. The ratio of the contributions by convective and radiative heat absorption was calculated from the simulation result. It should be noted that this kind of information can be hardly obtained from the measured data. It is observed that the contribution by the radiative heat transfer to the total amount of heat transfer is quite large for the water wall, whereas that is not so large for the plate and the 2nd superheaters. This is due to that the large part of the water wall is exposed to the strong heat radiation from the burner

zone, while the area being exposed to the radiation from the burner zone for the superheaters is small compared to the water wall.

Table 4 and Fig. 6 show the quantities of the convection heat transfer and the radiation heat transfer calculated from the simulation result, and three dimensional views for the heat flux distribution of superheater and reheater. It is observed from Table 4 that the quantity of the radiation heat transfer is larger than that of the convection heat transfer for the plate superheater. However, the quantity of the radiation heat transfer is smaller than that of the convection heat transfer for the 2nd superheater and the 1st reheater. The large quantity of the radiation heat transfer for the plate superheater is mainly caused by the strong radiation from coal particles with high temperature. This point can be understood from the slanted heat flux distribution of the plate superheater shown in Fig. 6. The heat flux of the area of the plate superheater in the side near to the burner zone is significantly higher than that in the opposite side (the side far from the burner zone). Since the plate superheater is exposed to the burner zone (See Fig. 1 (a)), the strong radiation from the burner zone directly reaches to the plate superheater. On the other hand, the quantity of the radiation heat transfer is small compared to that of the convection heat transfer for the 2nd superheater and the 1st reheater in Table 4. This is caused by that the 2nd superheater and the 1st reheater are not exposed to the burner zone (See Fig. 1 (a)), i.e., the strong radiation from the burner zone cannot directly reach to the 2nd superheater and the 1st reheater. Consequently, for the 2nd superheater and the 1st reheater, the maximum heat flux area is observed in the middle part of heaters where the gas velocity is high, while the maximum heat flux is observed in the side neat to the burner zone for the plate superheater.

3.2 Effect of the furnace scale on particle's thermal history

In this section, the effect of the furnace scale on the heat transfer of coal particles is discussed in detail using the calculated particle data for the three different scale furnaces.

Figure 7 shows the calculated particle residence time with the particle temperature above 1750 K, $t_{p,1750K}$, and the calculated particle residence time passing the gas with temperature above 1750 K, $t_{g,1750K}$ with various initial particle diameters. It is observed that $t_{g,1750K}$ for the 2.4 MW_{th} and 0.76 MW_{th} test furnaces decreases with increasing particle diameter, while that for the 915 MW_{th} boiler is almost constant. It is also observed that $t_{p,1750K}$ for the 2.4 MW_{th} and 0.76 MW_{th} test furnaces drastically decreases with increasing particle diameter, while the decrease in $t_{p,1750K}$ with particle diameter for the 915 MW_{th} boiler is smaller than that for the test furnaces. This means that the dependence of residence time with high particle temperature on the particle diameter for the small test furnaces is greater than that for the large scale furnace. This point is clearly shown in Fig. 8.

Figure 8 shows the ratio of $t_{p,1750K}$ to $t_{g,1750K}$ as a function of the initial particle diameter. It is observed that there is little difference in $t_{p,1750K}/t_{g,1750K}$ for the initial particle diameter of 5 μm between the furnaces. However, the difference in $t_{p,1750K}/t_{g,1750K}$ between the 915 MW_{th} boiler and the test furnaces increases with increasing initial particle diameter. This large difference in $t_{p,1750K}/t_{g,1750K}$ due to the furnace scale causes the difference in the fly ash particle shape as described in the next paragraph.

Figure 9 shows the relationship between S_{Ab}/S_{Ad} value and the surface mean diameter, $D_{s\text{-}ash}$ for the

2.4 MW_{th} test furnace and actual large scale boilers (different boilers from the 915 MW_{th} boiler in this study) taken from the study conducted by Shirai et al. [48]. S_{Ab} is the specific surface area of the ash measured by the Blaine method [49] and S_{Ad} is the specific surface area calculated from the ash particle size distribution and ash density on the assumption that ash particles are spherical. Increase in S_{Ab}/S_{Ad} means a decrease in the sphericity of the particles. Solid circles indicate S_{Ab}/S_{Ad} for the 2.4 MW_{th} test furnace and other plots indicate for the actual large scale boilers. It is observed that S_{Ab}/S_{Ad} for the 2.4 MW_{th} test furnace is larger than that for the large scale boilers. Even though various coals were used for both the 2.4 MW_{th} test furnace and the large scale boilers, the plots for the test furnace and the large scale boilers are completely separated, i.e., the inclination of S_{Ab}/S_{Ad} with the increase in $D_{s\text{-}ash}$ for the test furnace is obviously higher than that for the large scale boilers. In other words, discrepancy of S_{Ab}/S_{Ad} caused by the difference in coal brand or the difference in unit of large scale boilers is smaller than the effect of the furnace scale on S_{Ab}/S_{Ad}. Shirai et al. presumed that this was because the residence time of ash particles in the high-temperature zone in the small test furnace was shorter than that in the large scale boilers. By taking into account the results from the current numerical study, however, there is no significant difference in the particle residence time passing the high temperature gas between the 2.4 MW_{th} test furnace and the large scale boiler as shown in Fig. 7. The difference in S_{Ab}/S_{Ad} between the 2.4 MW_{th} test furnace and the large scale boiler is considered due to the difference in the particle residence time with the high particle temperatures as shown in Figs. 8 and 9. In the next section, the cause of the difference in $t_{p,1750K}/t_{g,1750K}$ between the 915 MW_{th} boiler and the test furnaces is discussed.

3.3 Effect of the furnace scale on the heat transfer mechanism of coal particles

Figure 10 shows the heat loss by devolatilization of the particles while the particles are passing gas with temperature above 1750 K normalized by initial particle mass, $HL_{dev,1750K}$ as a function of the initial particle diameter. It is found that $HL_{dev,1750K}$ increases with increasing particle diameter for all cases. This indicates that the large particles tend to enter the flame zone before the volatile matter is completely evolved from the particles. This is caused by the fact that the specific surface area of particle decreases with increasing particle diameter, i.e., the larger particles need more time to be heated up and evolve the volatile matter because of the smaller specific area. The heat loss by the devolatilization causes the particles to keep its temperature low. This is the reason why $t_{p,1750K}/t_{g,1750K}$ decreases with increasing particle diameter, as shown in Fig. 8. It is also found that the difference in $HL_{dev,1750K}$ between the 915 MW_{th} boiler and the test furnaces increases with increasing particle diameter. This is the cause of the tendency that the difference in $t_{p,1750K}/t_{g,1750K}$ between the 915 MW_{th} boiler and the test furnaces increases with increasing particle diameter, as shown in Fig. 8.

Figure 11 shows the ratio of the heat loss by devolatilization to the net heat gain of particles while particles are passing gas with temperature above 1750 K, $HL_{dev,1750K}/Q_{net,1750K}$ as a function of the initial particle diameter. Although a tendency of this graph is just same as that of Fig. 10, the significance of $HL_{dev,1750K}$ can be examined through this graph. It is found that the values of $HL_{dev,1750K}/Q_{net,1750K}$ for particles with the initial particle diameter of 100 μm for two test furnaces are more than 0.3, and these values are large enough to affect $t_{p,1750K}/t_{g,1750K}$ in Fig. 8. In other words, it

is also confirmed from Fig. 11 that the main cause of the tendency that the difference in $t_{p,1750K}/t_{g,1750K}$ between the 915 MW_{th} boiler and the test furnaces increases with increasing particle diameter is the increase of the difference in $HL_{dev,1750K}$ between the boilers. In the following part, the reason why the difference in $HL_{dev,1750K}$ between the 915 MW_{th} boiler and the test furnaces increases with increasing initial particle diameter is discussed.

As expressed by the Eq. (2.6), the particle temperature T_p is calculated by considering the heat transfer due to convection, radiation, the heat losses due to the evaporation of moisture and the devolatilization, and the heat gain due to char combustion. $HL_{dev,1750K}$ is controlled by the net heat gain of particles before the particles enter the high temperature gas region. Therefore, the heat transfer due to the convection or the radiation should control the value of $HL_{dev,1750K}$.

Figure 12 shows the gas velocity magnitude distributions in the furnaces. It is observed that the gas velocity magnitude in the 915 MW_{th} boiler is larger than that in the 2.4 MW_{th} and 0.76 MW_{th} test furnaces. This can affect the convection heat transfer coefficient, h, in Eq. (2.6).

Figure 13 shows the time-averaged convection heat transfer coefficient, h, in the three furnaces as a function of the initial particle diameter. h was calculated by Eqs. (2.7) and (2.8). It is observed that h decreases drastically with increasing particle diameter. This tendency can be understood by the existence of the particle diameter in the denominator of RHS of Eq. (2.7). Althouth h in the 915 MW_{th} boiler is slightly larger than that in the 2.4 MW_{th} and 0.76 MW_{th} test furnaces, the difference in h between three furnaces is not significant compared to the significant difference in $HL_{dev,1750K}$ of large particles between the 915 MW_{th} boiler and the test furnaces. Therefore, it is considered that the

difference in h is not the main cause of the difference in $t_{p,1750K}/t_{g,1750K}$ between the furnaces.

Figures 14 and 15 show the integrated heat gain of particles by radiation heat transfer normalized by the initial particle mass, HG_{rad}, and the integrated heat loss from particles by radiation heat transfer normalized by the initial particle mass, HL_{rad}, as a function of the initial particle diameter. It is observed in Fig. 14 that HG_{rad}, for the 915 MW_{th} boiler is significantly greater than that for the 2.4 MW_{th} and 0.76 MW_{th} test furnaces. On the other hand, HL_{rad} for the 915 MW_{th} boiler is smaller than that for the 2.4 MW_{th} and 0.76 MW_{th} test furnaces. These trends can be considered as a main cause of the difference in $HL_{dev,1750K}$ between the furnaces in Fig. 10. The lower HG_{rad} and higher HL_{rad} for the small test furnaces are due to the larger heat exchange between particles and cold furnace wall by radiation heat transfer than that for the large scale boiler because the flame thickness for the test furnaces is thinner than that for the large scale boiler. Particles in the 915 MW_{th} boiler tend to easily gain heat by radiation heat transfer from the large thick flame compared to that in the small test furnaces. For large particles, the lower HG_{rad} for small test furnaces causes the higher $HL_{dev,1750K}$ because the large amount of volatile matter remains in the particles before entering the flame zone due to the lower heat gain, although the volatile matter in small particles can be easily evolved because of large heat gain due to the large specific surface area of the small particles. This is why the difference in $HL_{dev,1750K}$ between the 915 MW_{th} boiler and the test furnaces increases with increasing initial particle diameter as shown in Fig. 10. The difference in $HL_{dev,1750K}$ between furnaces causes the difference in $t_{p,1750K}/t_{g,1750K}$ between the furnaces, as discussed previously.

From the above discussion, it is clarified that the particle residence time with the high particle

temperature for a small scale furnace is shorter than that for a large scale furnace even if the particle residence time passing the high temperature gas is the same. The difference in the particle residence time with the high particle temperature caused by the furnace scale is increased with increasing particle diameter. It should be noticed that the above consideration is necessary to evaluate the usability of coal brands in the viewpoint of the fly ash properties for actual large scale boilers by using the experimental data from small scale experimental apparatus, because the ash properties are significantly affected by the scale of furnace as clarified by this study.

4. Conclusions

In this study, the numerical simulations of coal combustion fields in the three different scale furnaces were conducted to investigate the effect of the furnace scale on the heat transfer mechanism of coal particles. The simulation results are compared to the measured data to validate the accuracy of the numerical simulation for the large scale boiler. As a result, it is concluded that the simulation could qualitatively reproduce the tendency of the O_2 concentration at the water wall. In addition to that, the simulation could quantitatively predict the heat absorption of the water wall, plate and 2nd superheaters. Finally, the effect of the furnace scale on the heat transfer mechanism of the particles was investigated by comparing the particle data between three furnaces statistically. The principal findings were as follows.

1. The particle residence time with high particle temperature for a small scale furnace is shorter than that for a large scale furnace even if the particle residence time passing the high

temperature gas is the same. This is caused by the larger heat loss due to the devolatilization of particles in the high temperature region for a small scale furnace. The lager heat loss due to the devolatilization is caused by the insufficient heat gain before the particles enter the high temperature gas for a small furnace.

2. The insufficient heat gain of particles for a small scale furnace is due to the lower radiation heat transfer because of the thinner flame thickness in the small furnace.
3. The difference in the particle residence time with high particle temperature causes the difference in the shape of ash particles collected from the exhaust gas. The sphericity of ash particles from small scale furnaces is lower than that from large scale furnaces because of the shorter particle residence time with high particle temperature. The difference in the sphericity due to the furnace scale increases with increasing particle diameter because the difference in the particle residence time with high particle temperature increases with increasing particle diameter.

Acknowledgments

The authors are indebted to whom it may concern in the electric power company operating the 915 MW_{th} boiler.

References

[1] Belošević S, Tomanović I, Beljanski V, Tucaković D, Živanović T. Numerical prediction of

processes for clean and efficient combustion of pulverized coal in power plants. Applied Thermal Eng 2015;74:102-10.
[2] Constenla I, Ferrín JL, Saavedra L. Numerical study of a 350 MWe tangentially fired pulverized coal furnace of the As Pontes power plant. Fuel Processing Tech 2013;116:189-200.
[3] Hwang M, Kim S, Kim G, Lee B, Song J, Park M, Jeon C. Simulation studies on direct ash recycling and reburning technology in a tangentially fired 500 MW pulverized coal boiler. Fuel 2013;114:78-87.
[4] Al-Abbas AH, Naser J, Hussein EK. Numerical simulation of brown coal combustion in a 550 MW tangentially-fired furnace under different operating conditions. Fuel 2013;107:688-98.
[5] Gubba SR, Ingham DB, Larsen KJ, Ma L, Pourkashanian M, Tan HZ, Williams A, Zhou H. Numerical modelling of the co-firing of pulverised coal and straw in a 300 MWe tangentially fired boiler. Fuel Processing Tech 2012;104:181-8.
[6] Belosevic S, Beljanski V, Tomanovic I, Crnomarkovic N, Tucakovic D, Zivanovic T. Numerical analysis of NOx control by combustion modifications in pulverized coal utility boiler. Energy Fuels 2012;26:425-42.
[7] Fang Q, Wang H, Wei Y, Lei L, Duan X, Zhou H. Numerical simulations of the slagging characteristics in a down-fired, pulverized-coal boiler furnace. Fuel Processing Tech 2010;91:88-96.
[8] Modlinski, N. Computational modeling of a utility boiler tangentially-fired furnace retrofitted with swirl burners. Fuel Processing Tech 2010;91:1601-8.
[9] Pallarés J, Gil A, Cortés C, Herce C. Numerical study of co-firing coal and Cynara cardunculus in a 350 MWe utility boiler. Fuel Processing Tech 2009;90:1207-13.
[10] Hashimoto N, Hwang SM, Kurose R, Tsuji H, Shirai H. A numerical simulation of pulverized coal combustion employing a tabulated-devolatilization-process model (TDP model). Combust Flame 2012;159:353-66.
[11] Hashimoto N, Kurose R, Shirai H. Numerical simulation of pulverized coal jet flame employing the TDP model. Fuel 2012;97:277-87.
[12] Umetsu H, Watanabe H, Kajitani S, Umemoto S. Analysis and modeling of char particle combustion with heat and multicomponent mass transfer. Combust. Flame 2014;161:2177-91.
[13] Ikeda M, Makino H, Morinaga H, Higashiyama K, Kozai Y. Emission characteristics of NOx and unburned carbon in fly ash during combustion of blends of bituminous/sub-bituminous coals. Fuel 2003;82:1851-7.
[14] Hashimoto N, Shirai H. Numerical simulation of sub-bituminous coal and bituminous coal mixed combustion employing TDP model. Energy 2014;71:399-413.
[15] Tsuji H, Shirai H, Matsuda H, Rajoo P. Emission characteristics of NOx and unburned carbon in fly ash on high-ash coal combustion. Fuel 2011;90:850-3.
[16] Kurose R, Ikeda M, Makino H. Combustion characteristics of high ash coal in a pulverized coal combustion. Fuel 2001;80:1447-55.
[17] Shirai H, Ikeda M, Aramaki H. Characteristics of hydrogen sulfide formation in pulverized coal

combustion. Fuel 2013;114:114-9.
[18] Hayashi J, Hashimoto N, Nakatsuka N, Tsuji H, Watanabe H, Makino H, Akamatsu F. Soot formation characteristics in a lab-scale turbulent pulverized coal flame with simultaneous planar measurements of laser induced incandescence of soot and Mie scattering of pulverized coal. Proc Combust Inst 2013;34:2435-43.
[19] Shirai H, Tsuji H, Ikeda M, Kotsuji T. Influence of combustion conditions and coal properties on physical properties of fly ash generated from pulverized coal combustion. Energy & Fuels 2009;23:3406-11.
[20] Watanabe H, Kurose R, Komori S. Large-eddy simulation of swirling flows in a pulverized coal combustion furnace with a complex burner. J Environment Eng 2009;4:1-11.
[21] Yoshiie R, Hikosaka N, Nunome Y, Ueki Y, Naruse I. Effects of flue gas re-circulation and nitrogen contents in coal on NO_X emissions under oxy-fuel coal combustion. Fuel Processing Tech 2014;136:106-11.
[22] Noda N, Ito S, Nunome Y, Ueki Y, Yoshiie R, Naruse I. Volatilization characteristics of boron compounds during coal combustion. Proc Combust Inst 2013;34:2831-8.
[23] Hwang SM, Kurose R, Akamatsu F, Tsuji H, Makino H, Katsuki M. Application of optical diagnostics techniques to a laboratory-scale turbulent pulverized coal flame. Energy & Fuels 2005;19:382-92.
[24] Balusamy S, Schmidt A, Hochgreb S. Flow field measurements of pulverized coal combustion using optical diagnostic techniques. Exp Fluids 2013;54:1534–48.
[25] Muto M, Watanabe H, Kurose R, Komori S, Balusamy S, Hochgreb S. Large-eddy simulation of pulverized coal jet flame - Effect of oxygen concentration on NOx formation. Fuel 2015;142:152-63.
[26] Stadler H, Ristic D, Förster M, Schuster A, Kneer R, Scheffknecht G. NO_x-emissions from flameless coal combustion in air, Ar/O_2 and CO_2/O_2. Proc Combust Inst 2009;32:3131-8.
[27] Habermehl M, Erfurth J, Toporov D, Förster M, Kneer R. Experimental and numerical investigations on a swirl oxycoal flame. Applied Thermal Eng 2012;49:161-9.
[28] Smart JP, Patel R, Riley GS. Oxy-fuel combustion of coal and biomass, the effect on radiative and convective heat transfer and burnout. Combust Flame 2010;157:2230-40.
[29] Kurose R, Makino H, Suzuki A. Numerical analysis of pulverized coal combustion characteristics using advanced low-NOx burner. Fuel 2004;83:693-703.
[30] Watanabe H, Tanno K, Baba Y, Kurose R, Komori S. Large-eddy simulation of coal combustion in a pulverized coal combustion furnace with a complex burner, Turbu Heat Mass Trans 2009;6:1027-30.
[31] Kurose R, Watanabe H, Makino H. Numerical simulations of pulverized coal combustion, KONA Pow Parti J 2009;27:144-56.
[32] Olenik G, Stein OT, Kronenburg A. LES of swirl-stabilised pulverised coal combustion in IFRF furnace No. 1. Proc Combust Inst. 2015;35:2819-28.
[33] Hashimoto N, Kurose R, Tsuji H, Shirai H. A numerical analysis of pulverized coal combustion

in a multiburner furnace. Energy & Fuels 2007;21:1950-8.
[34] Yakhot V, Orszag SA. Renormalization group analysis of turbulence. I. Basic theory. J Scientific Computing 1986;1:3-51.
[35] Siegel R, Howell J. Thermal Radiation Heat Transfer. 4th ed. New York: Taylor & Francis; 2002, p. 681-95.
[36] Magnussen BF, Hjertager BH. On mathematical modeling of turbulent combustion with special emphasis on soot formation and combustion. Proc Combust Inst 1977;16:719-29.
[37] Field MA. Rate of combustion of size-graded fractions of char from a low-rank coal between 1200°K and 2000°K. Combust Flame 1969;13:237-52.
[38] Essenhigh RH, Klimesh HE, Förtsch D. Combustion characteristics of carbon: Dependence of the Zone I-Zone II transition temperature (T_c) on particle radius. Energy & Fuels 1999;13:826-31.
[39] Gosman AD, Ioannides E. Aspects of computer simulation of liquid-fuelled combustors. AIAA paper 1981: No. 81-0323.
[40] Issa RI, Solution of the implicitly discretised fluid flow equations by operator-splitting. Comp Phys 1986;62:40-65.
[41] Schiller L, Naumann Z. A drag coefficient correlation. Z Ver Deutsch Ing, 1935;77:318-20.
[42] El Wakil MM, Uyehara OA, Myers PS. A theoretical investigation of the heating-up period of injected fuel droplets vaporizing in air. NACA Technical Note 3179, Washington, DC, 1954.
[43] Crowe CT, Sharma MP, Stock DE. Particle-source-in cell (PSI-cell) model for gas-droplet flows. Trans ASME J Fluids Eng 1977;99:325-32.
[44] Niksa S. Predicting the devolatilization behavior of any coal from its ultimate analysis. Combust Flame 1995;100:384-94.
[45] Niksa S, Kerstein AR. FLASHCHAIN theory for rapid coal devolatilization kinetics. 1. Formulation. Energy & Fuels 1991;5:647-65.
[46] Westbrook CK, Dryer FL. Simplified reaction mechanisms for the oxidation of hydrocarbon fuel in flames. Combust Sci Tech 1981;27:31-43.
[47] Hautman DJ, Dryer FL, Schug KP, Glassman I. A multiple-step overall kinetic mechanism for the oxidation of hydrocarbons. Combust Sci Tech 1981;25:219-35.
[48] Shirai H, Ikeda M, Tanno K. Factors affecting the density and specific surface area (Blaine value) of fly ash from pulverized coal combustion. Energy & Fuels 2011;25:5700-6.
[49] Japanese Industrial Standard (JIS) JIS R 5201; JIS: Tokyo, Japan, 1997.

Figure and table captions

Fig. 1 Outlines of computational domains.

Fig. 2 Calculated streamlines in 915 MW_{th} boiler. Colors of streamlines indicate (a) O_2 concentration and (b) gas temperature, respectively.

Fig. 3 Distributions of gas temperature and O_2 concentration on cross section at center of center burners for 915 MW_{th} boiler.

Fig. 4 Comparison of O_2 concentration at inspection windows and calculated O_2 concentration on furnace wall surface for the 915 MWth boiler.

Fig. 5 Quantity of heat transfer for 915 MWth boiler.

Fig. 6 Three dimensional views for heat flux distribution of superheater and reheater.

Fig. 7 Particle residence time with particle temperature above 1750 K, $t_{p,1750K}$, and particle residence time passing gas with temperature above 1750 K, $t_{g,1750K}$.

Fig. 8 Ratio of particle residence time with particle temperature above 1750 K, $t_{p,1750K}$, to particle residence time passing gas with temperature above 1750 K, $t_{g,1750K}$.

Fig. 9 S_{Ab}/S_{Ad} value as a function of $D_{s\text{-}ash}$ for 2.4 MW_{th} test furnace and other actual large scale boilers [48]. Reprinted with permission from ref. [48]. Copyright 2011 American Chemical Society.

Fig. 10 Heat loss by devolatilization of the particles while the particles are passing gas with temperature above 1750 K normalized by initial particle mass.

Fig. 11 Ratio of the heat loss by devolatilization to net heat gain of particles while particles are passing gas with temperature above 1750 K.

Fig. 12 Gas velocity magnitude distributions in furnaces.

Fig. 13 Time-averaged convection heat transfer coefficient of particles in furnaces.

Fig. 14 Integrated heat gain of particles by radiation heat transfer normalized by initial particle mass.

Fig. 15 Integrated heat loss from particles by radiation heat transfer normalized by initial particle mass.

Table 1 Summary of mathematical models used in simulation.

Table 2 Specification of furnaces.

Table 3 Coal properties.

Table 4 Calculated quantities of convection and radiation heat transfers from simulation result.

Table 1. Summary of mathematical models used in simulation.

Phenomena	Mathematical model
Turbulence	RNG k-ε [34]
Thermal Radiation	Discrete Ordinate [35]
Devolatilization	Modified TDP model [14]
Gas phase combustion	Combined model of kinetics and eddy dissipation [36]
Char combustion	Field et al. [37]
Char combustion zone transition	Essenhigh et al. [38]
Particle's tracking	Lagrangian
Turbulence effect on particle motion	Stochastic [39]

Table 2. Specification of furnaces.

Furnace	Thermal input [MW]	The number of burners	Residence time in the furnace [s]	O_2 mole fraction at furnace exit
915 MW_{th} boiler	810	30	4	0.04
2.4 MW_{th} test furnace	2.4	3	4	0.04
0.76 MW_{th} test furnace	0.76	1	4	0.04

Table 3. Coal properties.

Coal	Coal A	Coal B
Proximate analysis [wt.%]		
Moisture (as-received)	8.9	22.1
Moisutre (after pulverized)	1.6	4.9
Volatile matter*	35.3	47.9
Fixed carbon*	53.0	47.8
Ash*	11.7	4.4
Fuel ratio [-]	1.50	1.00
Ultimate analysis* [wt.%]		
C	74.3	66.7
H	5.0	5.5
N	1.5	1.2
O	7.0	22.3
Combustible sulfur	0.5	0.1
Lower heating value (LHV)* [MJ/kg]	29.10	27.55
Mass fraction of particles [%]		
D_p = 5 μm	2.7	3.2
D_p = 20 μm	29.3	27.8
D_p = 40 μm	31.3	27.0
D_p = 60 μm	14.5	12.9
D_p = 80 μm	12.7	15.5
D_p = 100 μm	9.5	13.5

*Dry basis.

Table 4. Calculated quantities of convection and radiation heat transfers from simulation result.

	Quantity of heat transfer [MW]	
	Convection	Radiation
Plate superheater	22.0	46.2
2nd superheater	33.0	29.6
1st reheater	43.1	21.6

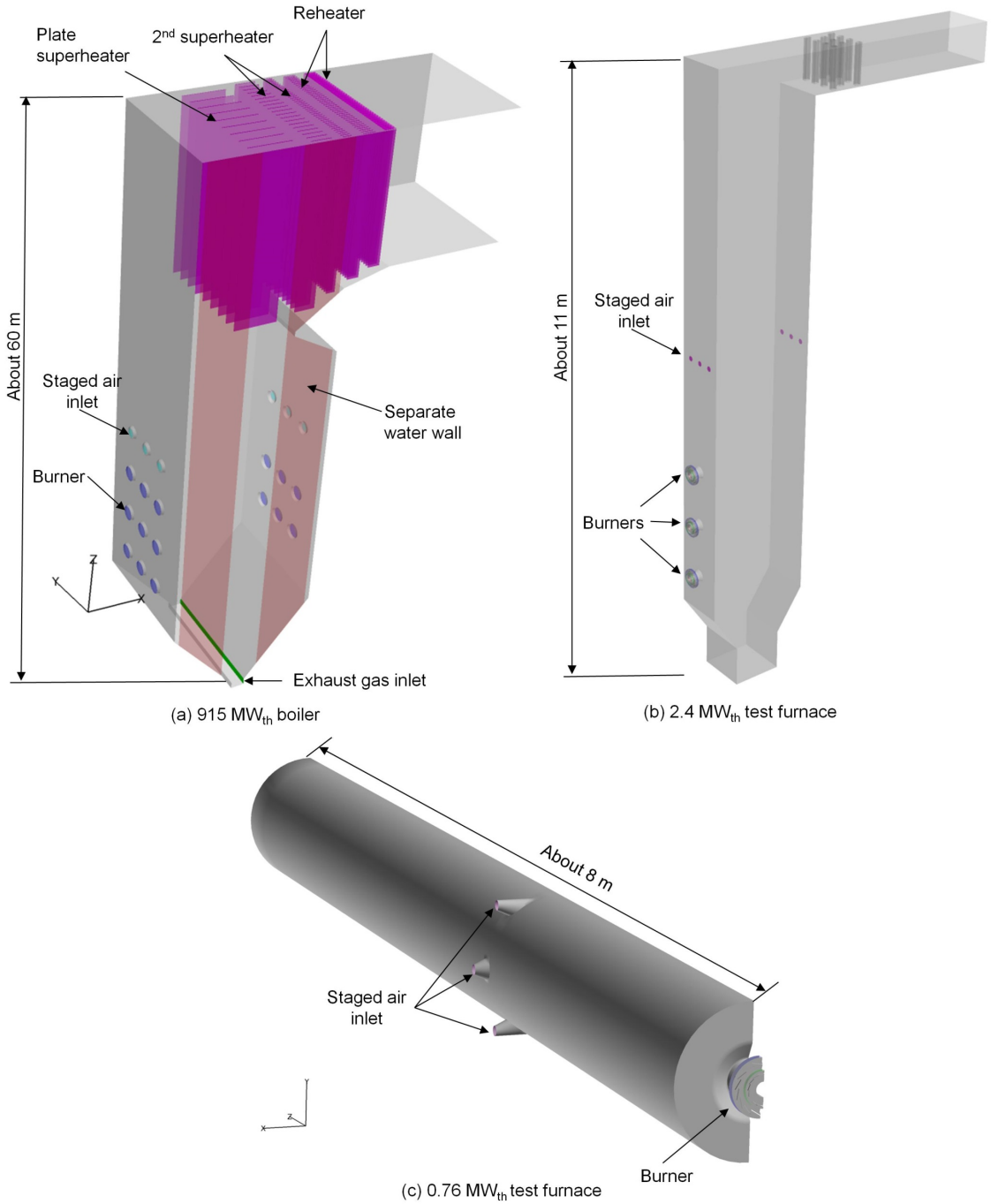

Fig. 1. Outlines of computational domains.

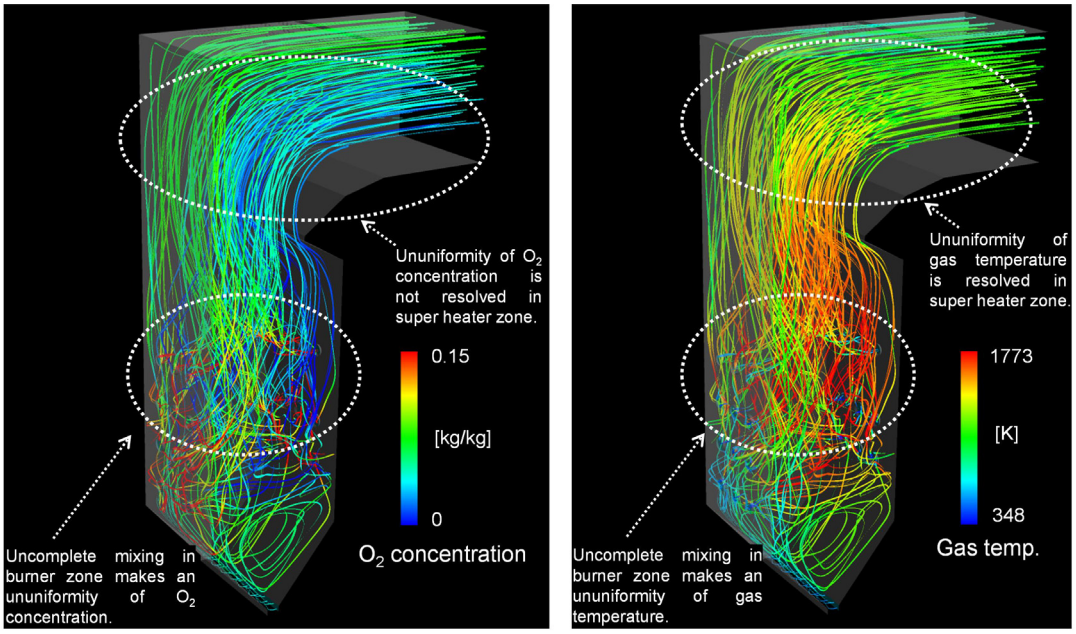

(a) O_2 concentration on streamlines (b) Gas temperature on streamlines

Fig. 2. Calculated streamlines in 915 MW_{th} boiler with (a) O_2 concentration and (b) gas temperature.

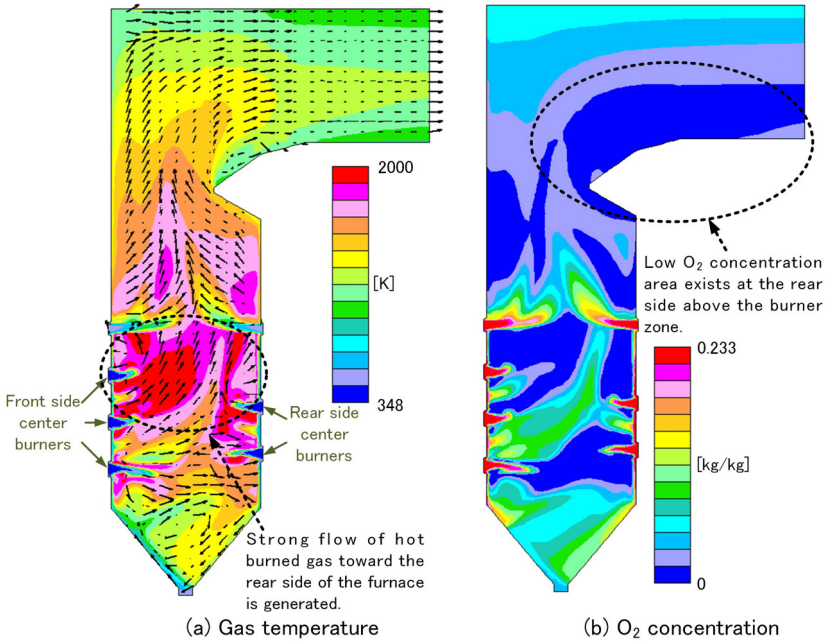

Fig. 3. Distributions of gas temperature and O_2 concentration on cross section at center of center burners for 915 MW_{th} boiler.

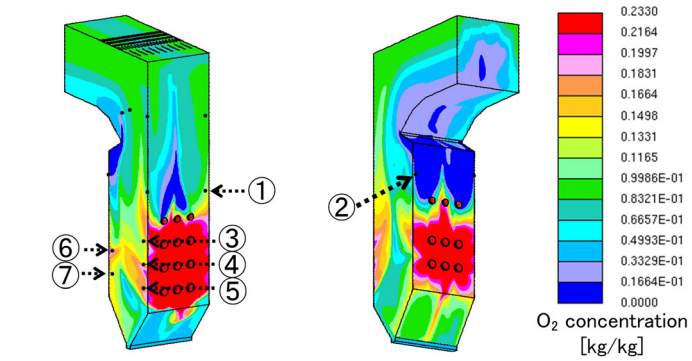

(a) Calculated O_2 concentration on furnace wall surface and positions of inspection windows

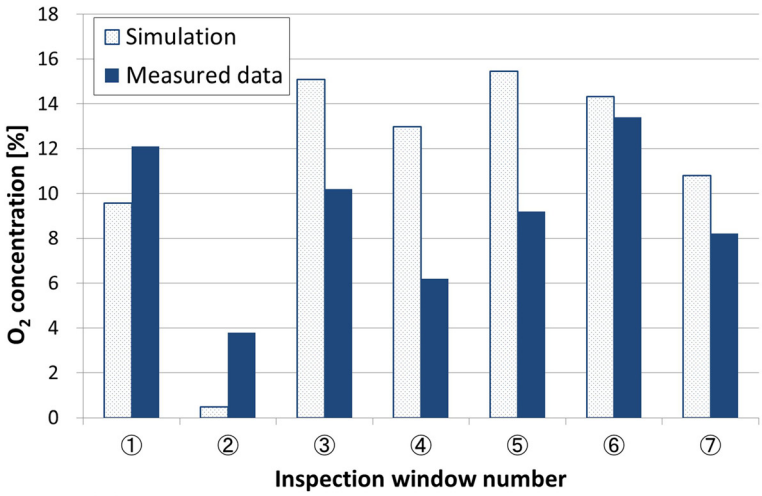

(b) O_2 concentration at inspection windows

Fig. 4. Comparison of O_2 concentration at inspection windows and calculated O_2 concentration on furnace wall surface for the 915 MW_{th} boiler.

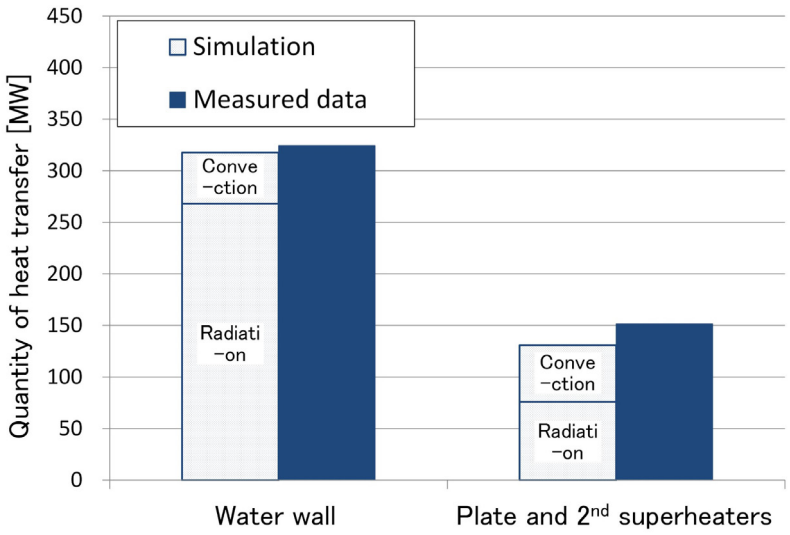

Fig. 5. Quantity of heat transfer for 915 MW_{th} boiler.

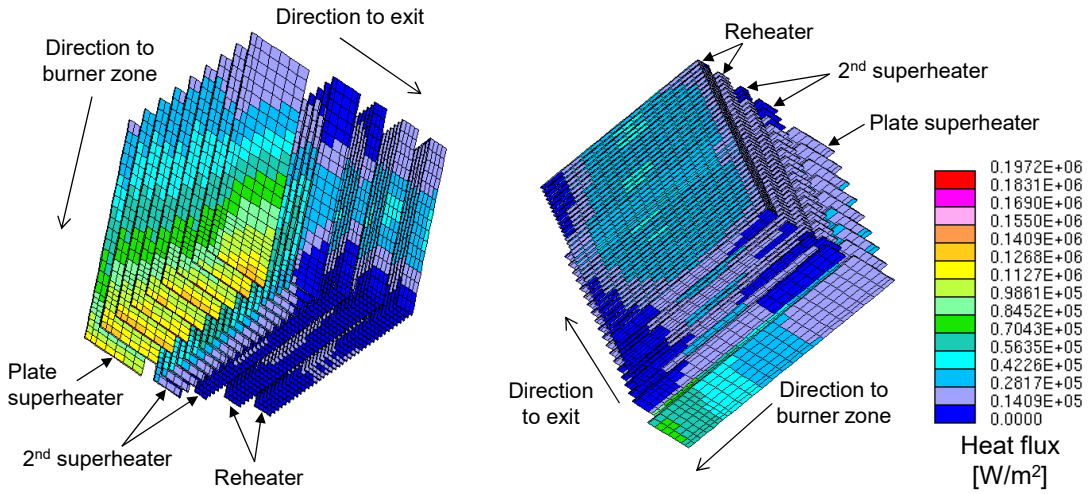

(a) View from furnace bottom direction (b) View from furnace exit direction

Fig. 6. Three dimensional views for heat flux distribution of superheater and reheater.

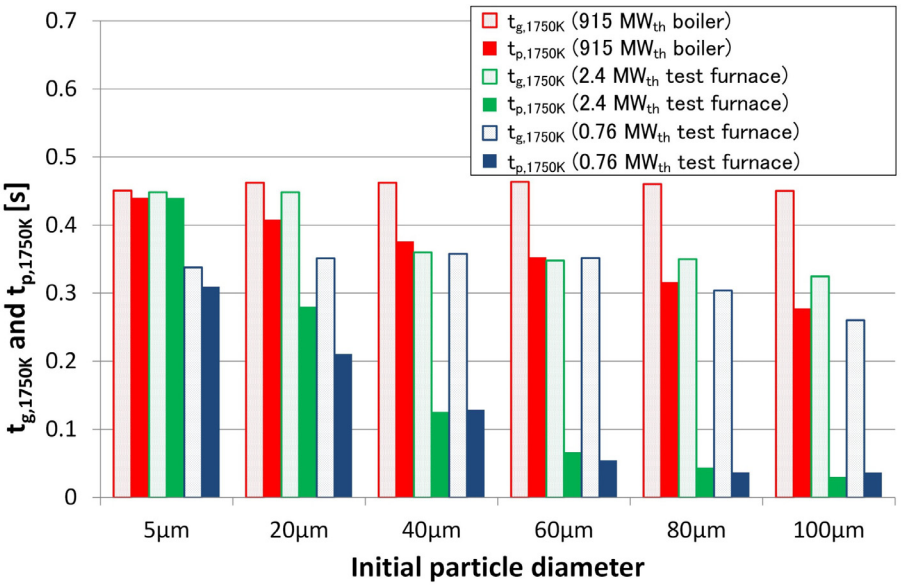

Fig. 7. Particle residence time with particle temperature above 1750 K, $t_{p,1750K}$, and particle residence time passing gas with temperature above 1750 K, $t_{g,1750K}$.

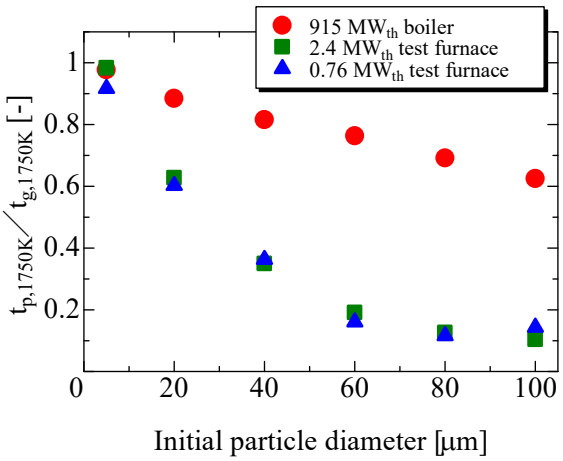

Fig. 8. Ratio of particle residence time with particle temperature above 1750 K, $t_{p,1750K}$, to particle residence time passing gas with temperature above 1750 K, $t_{g,1750K}$.

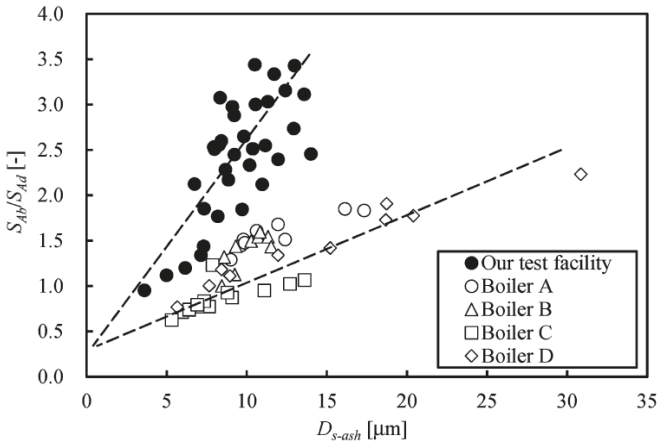

Fig. 9. S_{Ab}/S_{Ad} value as a function of $D_{s\text{-}ash}$ for 2.4 MW_{th} test furnace and other actual large scale boilers [48]. Reprinted with permission from ref. [48]. Copyright 2011 American Chemical Society.

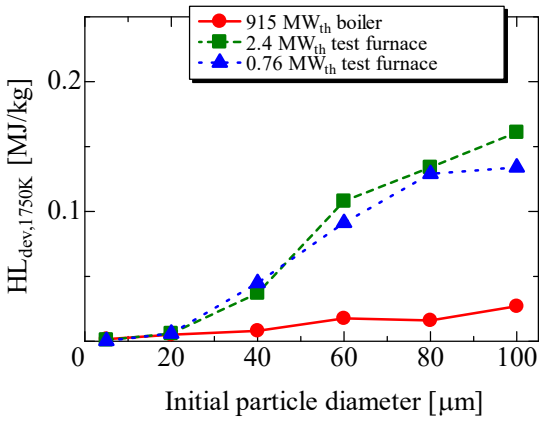

Fig. 10. Heat loss by devolatilization of the particles while the particles are passing gas with temperature above 1750 K normalized by initial particle mass.

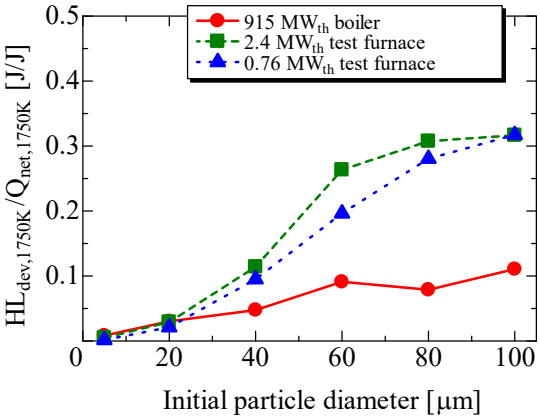

Fig. 11. Ratio of the heat loss by devolatilization to net heat gain of particles while particles are passing gas with temperature above 1750 K.

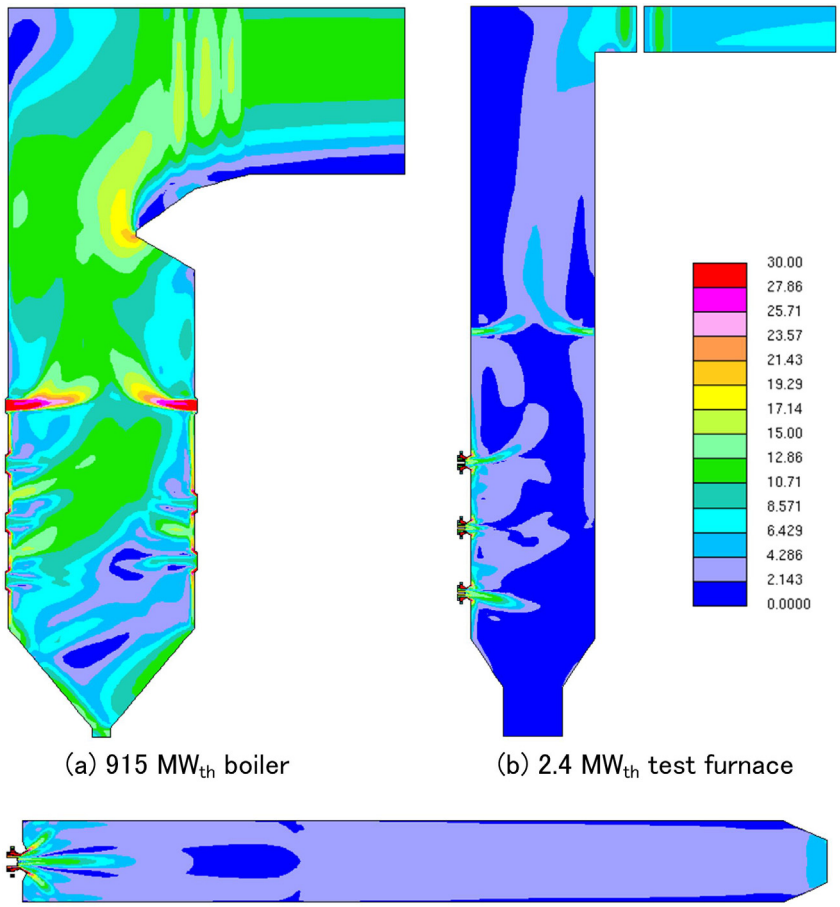

(a) 915 MW_{th} boiler

(b) 2.4 MW_{th} test furnace

(c) 0.76 MW_{th} test furnace

Fig. 12. Gas velocity magnitude distributions in furnaces.

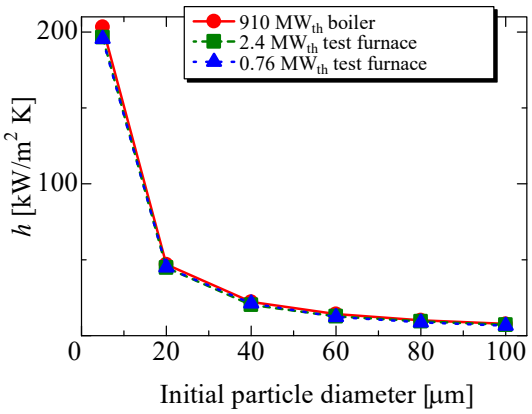

Fig. 13. Time-averaged convection heat transfer coefficient of particles in furnaces.

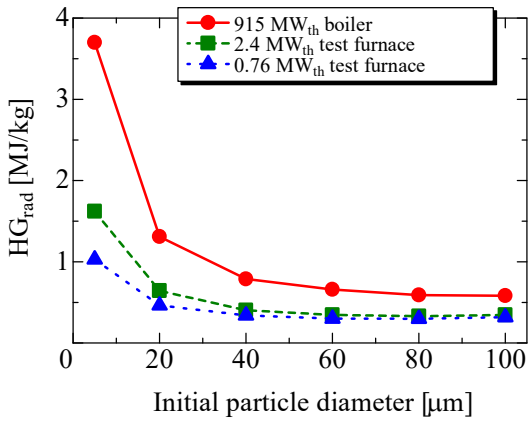

Fig. 14. Integrated heat gain of particles by radiation heat transfer normalized by initial particle mass.

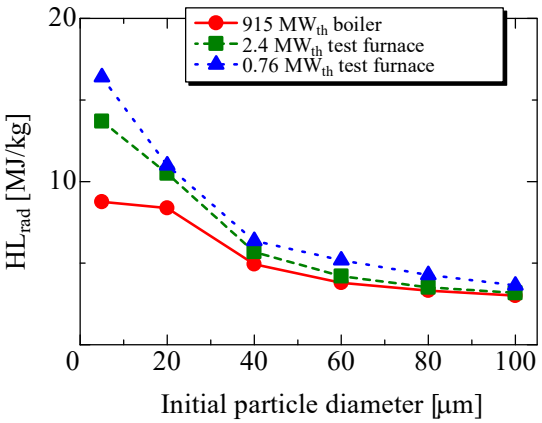

Fig. 15. Integrated heat loss from particles by radiation heat transfer normalized by initial particle mass.